

A Study of Ion Thruster Optics through Particle Simulations and Evaluation of the Near Plume Plasma Properties

Emre Turkoz*, Firat Sik† and Murat Celik‡

Bogazici University, Istanbul, 34342, Turkey

A three-dimensional hybrid PIC-DSMC code is developed to simulate the physics of ion optics between an accelerator and a screen grid that are placed at the end of the discharge chamber of an ion thruster. Ions and neutrals are both represented with macro particles that have different weights. Electric potential is evaluated from the Gauss' Law that takes the form of the Poisson's equation, where the right hand side includes the net charge density evaluated at the computational grid nodes. The solution domain is a 30° slice in cylindrical coordinates with symmetry boundary conditions at the radial and azimuthal boundaries. Macro particles are tracked with the Leapfrog algorithm. DSMC collisions are implemented for heavy species. A parametric study is performed to find the grid configuration that yields the best performance.

Nomenclature

\mathbf{r}	Particle position
\mathbf{v}	Particle velocity
\mathbf{a}	Particle acceleration
\mathbf{E}	Electric field
n	Number density
\mathbf{v}	Velocity field
ν	Collision frequency
r	Radial position
θ	Azimuthal position
z	Axial position
ϕ	Electric potential
P	Perveance
e	Elementary charge
<i>Subscript</i>	
∞	downstream
i	Ion species
n	Neutral species
e	Electron species

I. Introduction

ION optics is an important and essential area of research for electric propulsion in evaluating ion thruster performance. Its subject is to investigate the physics between the electrostatic grids that are located at the end of the discharge chamber to accelerate the charged ions out of the thruster to generate thrust. This work presents an indigenous modeling effort to simulate intra-grid and near plume plasma of an ion thruster.

*Graduate Student, Department of Mechanical Engineering, Bogazici University.

†Undergraduate Student, Department of Mechanical Engineering, Bogazici University.

‡Assistant Professor, Department of Mechanical Engineering, Bogazici University.

Electrostatic grids generally consist of two or three grid sets that are placed with small gaps in between. The two-grid design consists of a screen and an accelerator grid, whereas the three-grid design has a decelerator grid in addition to these two in order to increase thrust per unit area. A detailed introduction to the topic can be found in the literature.¹

In order to build a complete model of the ion thruster, in addition to the model for the discharge chamber, a model with the capability to handle the ion optics is needed. In the pursuit of building an RF ion thruster in our facilities,² a fluid model for the discharge plasma has already been developed.³ Now with this work the aim is to fill the gap by building an ion optics model. With the model developed within the scope of this work, the aim is to investigate the underlying physics of RF ion thrusters at the facilities built at Bogazici University Space Technologies Laboratory (BUST-Lab).

The physics of the intra-grid plasma is different from the discharge chamber plasma. A numerical model for the grid plasma should include the evaluation of the electric field imposed by the voltage difference between the grids. The quasi-neutrality inevitably breaks down when the ions are extracted from the discharge chamber due to this voltage difference. Electrons are strongly repelled again because of this field. Therefore a quasi-neutral plasma fluid model is not suitable to simulate the plasma in the grid region.

There are various ion optics models to be found in the literature. The first efforts in the field of ion optics^{4,5} focus on correlating the experiments with analytical formulations to estimate the lifetime and ion current of ion thrusters. With the advances in kinetic modeling and PIC-DSMC algorithms, ion optics simulations started to receive attention. Farnell⁶ has developed the ffx, an ion optics code that handles both particle motion and grid sputtering effects. CEX3D,⁷ an upgrade of CEX2D,⁸ developed at Jet Propulsion Laboratory, is capable of simulating the two-grid ion optics in three dimensions. Another model, igx,⁹ employs a useful approach for simulating the hexagonal grid patterns in three dimensions. This approach is also incorporated to the work presented in this paper. Recently a study on the time-dependent ion optics¹⁰ is performed that captures the effect of sputtering grids on the ion trajectories. A computational tool, JIEDI,¹¹ is developed by JAXA for ion optics simulations and thruster life time evaluations. A recent study with the JIEDI tool¹² investigates the effect of double ions on a specific thruster grid design.

Plasma particle simulations have many examples from the literature. Oh¹³ laid out the basics of the particle model for a quasi-neutral plasma. Fife¹⁴ developed a hybrid-PIC simulation scheme where the electrons are assumed to be fluid but remaining species are tracked by using particles. Szabo¹⁵ developed a fully kinetic model for plasma thrusters. According to the trend from the literature, the DSMC collisions between the heavy species, ions and neutrals, are implemented into this study. The implementation of the collision model in this work is inspired from Celik's work on plasma thruster plumes.¹⁶

This paper is organized as follows. Section II gives a brief summary of the theory developed for ion optics. Section IV explains the DSMC collision algorithm employed in this study. In Section III the numerical model used in this study is presented. The investigated problem configuration is given in Section V and results are presented in Section VI. Concluding remarks are given in Section VII.

II. Ion Optics Theory

Ion optics rely on the force that is generated through the electrostatic potential difference between two or more adjacent grids. The conventional designs consist of either a two-grid system or a three-grid system. For the initial development of the theory, a two-grid system is investigated which consists of a screen and an accelerator grid. A hole pair from screen and accelerator grids is shown in Figure 1.

The most important consideration in extracation grid design is the space-charge limitation. Space-charge limitation occurs due to the fact that ions directly affect the electric potential distribution. Ions normally "fall" over the potential drop that exists between the grids. But if ions are excessively present in the grid region, they affect the potential distribution and ions start not to see a potential drop. This effect is reflected in the governing equations. In the scope of a simple one-dimensional analysis, the Gauss' law is formulated as:

$$\frac{d^2\phi}{dx^2} = -\frac{en_i}{\epsilon_0} \quad (1)$$

where n_i is the ion number density, and ϵ_0 is the electric constant. It is seen that the contribution of the electrons to the net charge is neglected because of the existence of the high potential that reflects them. The ion number density can be expressed by defining the ion charge flux as:

$$en_i\mathbf{v}_i = \mathbf{J} \quad (2)$$

where \mathbf{J} is the current density and constant because of the current continuity. Also assuming that the whole potential energy is deposited into the ions:

$$\mathbf{v}_i = \sqrt{\frac{2e(-\Delta\phi)}{m_i}} \quad (3)$$

where m_i is the ion mass. Combining these equations yield a nonlinear differential equation for the electric potential with the following boundary conditions:

$$\phi(0) = 0, \quad \phi(x = d) = -V_a \quad (4)$$

It is also imposed that the electric field is zero on the screen grid due to space charge limitation:

$$\left(\frac{d\phi}{dx}\right)_{x=0} = 0 \quad (5)$$

Solution of the resulting nonlinear equation yields the Child-Langmuir space-charge limit, and it is formulated as:

$$\mathbf{J} = \frac{4\sqrt{2}}{9} \epsilon_0 \left(\frac{e}{m_i}\right) \frac{V_a^{3/2}}{l_g^2} \quad (6)$$

where l_g is the gap distance between the grids, and V_a is the electrostatic potential difference between the grids, which is also used in the boundary condition.

If the space-charge limited current density is multiplied by the beam area, the maximum possible current can be calculated. For a beam with diameter D , the current is formulated as:

$$\mathbf{I} = \frac{\pi D^2}{4} \mathbf{J} = \frac{\pi}{4} \frac{4\sqrt{2}}{9} \epsilon_0 \left(\frac{e}{m_i}\right) \frac{D^2}{l_g^2} V_a^{3/2} = P V_a^{3/2} \quad (7)$$

where P is called as the *perveance* of the extraction system. In past studies, it is laid out that this one-dimensional analysis is inadequate to predict the performance of actual grid system because the three-dimensional geometry effects are neglected. The following correction to calculate the perveance value is suggested:¹⁷

$$P = \frac{I_h}{V_a^{3/2}} \left(\frac{l_e}{d_s}\right) \quad (8)$$

where I_h is the beam current per hole, d_s is the screen grid aperture diameter and l_e is defined as:

$$l_e = \sqrt{l_g^2 + (d_s^2/4)} \quad (9)$$

A similar correction should be applied on the Child-Langmuir law itself to reach the correct values of the limiting current. The three-dimensional correction⁴ to this law is performed by replacing the square of the gap distance, l_g^2 , in Equation 6 with $(l_g + t_s)^2 + D_s^2/4$.

Another limiting factor in the extraction system design is the phenomenon named as electron backstreaming. Electron backstreaming occurs when the accelerator grid potential is so low that the grid starts to attract electrons coming out from the cathode that should normally neutralize the plume region. To work on electron backstreaming, a new parameter, R , is introduced to define the net-to-total potential ratio ($R = V_N/V_T$).

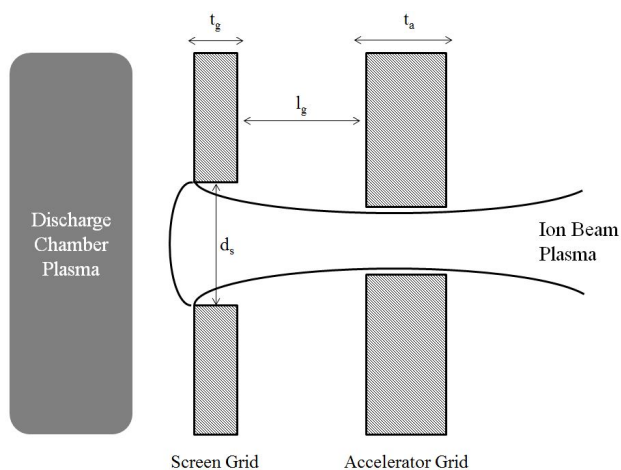


Figure 1. Representation of grid holes of the two-grid system¹⁷

The net-to-total potential ratio has a maximum value for the electron backstreaming not to take place. This maximum is formulated as follows:¹⁷

$$R_{max} = 1 - \frac{0.2}{(l_e/d_a)e^{(t_a/d_a)}} \quad (10)$$

This formula depends purely on the geometry, and proves to be a conservative estimate of the real laboratory conditions.

There is another factor to consider in addition to the electron backstreaming while adjusting the net-to-total potential ratio. Perveance tends to increase as this ratio increases. But after a certain R value, the impingement current becomes a limiting factor. The impingement current indicates the current that reaches the screen grid in two-grid systems, or the acceleration grid in three-grid systems.

III. Numerical Model

The numerical model consists of two major components. The first component is the solution of the electric potential equation to determine the electric field throughout the domain, and the second component is the particle tracking and application of collisions. Both components are affected by the chosen solution domain and the coordinate system.

In the considered design, grids are manufactured such that their holes are concentric with hexagons as shown in the Fig. 2. A grid consists of these hexagons that are aligned side by side. Because of this hexagonal pattern and geometry of the grids, cylindrical coordinates are employed in this study. A representation of the geometry where the plasma parameters are resolved in 3D is given in Fig. 2.

The equation solved to evaluate the electric potential distribution throughout the domain is the well-known Poisson's equation:

$$\nabla^2 \phi = -\frac{\rho}{\varepsilon_0} \quad (11)$$

where ρ is the net charge density and ε_0 is the permittivity of free space.

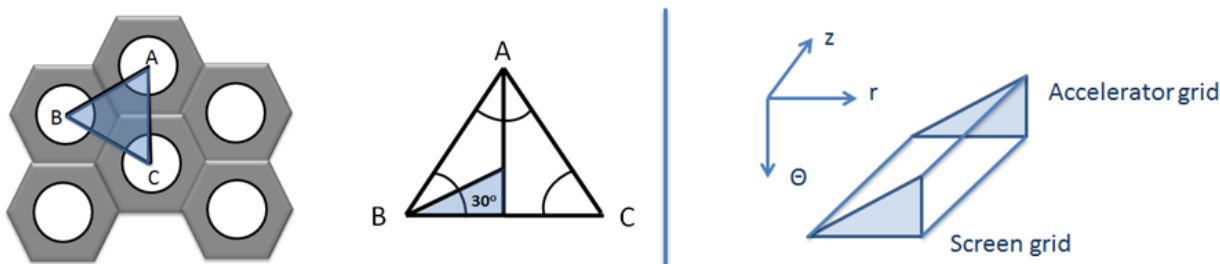


Figure 2. Ion grids geometry and the solution domain to be used in the model and presented with the introduction of the igx⁹ ion optics code

In the solution of the electric potential equation, a structured rectangular grid is used. The grid employed and an example boundary condition set is presented in Fig. 3. The same three dimensional computational grid is utilized for the particle tracking.

The electric potential equation (11) is extended to cylindrical coordinates as follows:

$$\nabla^2 \phi = \frac{1}{r} \frac{\partial}{\partial r} \left(r \frac{\partial \phi}{\partial r} \right) + \frac{1}{r^2} \frac{\partial^2 \phi}{\partial \theta^2} + \frac{\partial^2 \phi}{\partial z^2} = -\frac{\rho}{\varepsilon_0} \quad (12)$$

where r denotes the radial coordinate. The right hand side of the equation, the charge density, is calculated by weighting each macro particle's charge to the cell nodes. According to the weighting scheme employed in cylindrical coordinates, the accumulated charge at one node of the mesh is formulated as follows

$$\rho_n = \rho_n + \frac{q_p}{V_{cell}} \left(1 - \frac{|(z_n - z_p)\pi(r_n^2 - r_p^2)(\theta_n - \theta_p)|}{V_{cell}} \right) \quad (13)$$

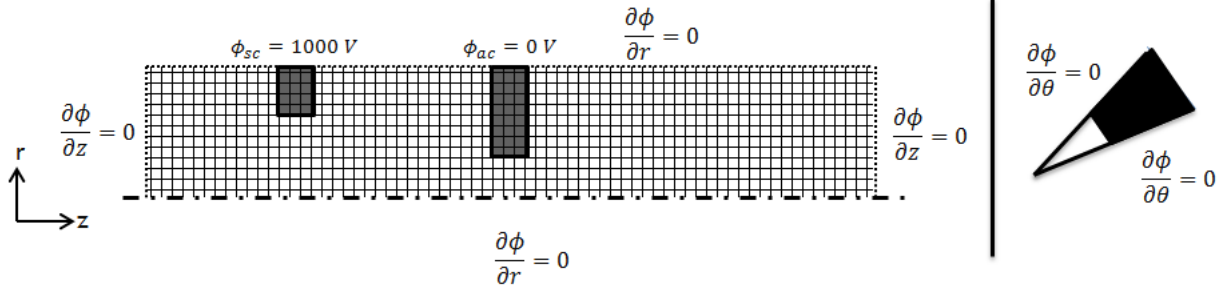


Figure 3. Solution domain: Electric potential equation is solved in 3D cylindrical coordinates on a wedge shaped domain with a 30° angle⁹

where ρ_n denotes the charge density of the node, q_p is the charge that the particle is carrying in Coulombs, and z , r and θ denotes the axial, radial and azimuthal coordinates, respectively. Using ρ_n in both sides of the equation indicates a summation over each particle which is located in a cell that harbors this node. The subscript p denotes the particle and the subscript n denotes the node considered. V_{cell} denotes the cell volume in cylindrical coordinates:

$$V_{cell} = \pi \Delta r (r_L + r_U) \Delta z \Delta \theta \quad (14)$$

where r_L is the radial position of the lower node, and r_U is the radial position of the upper node of the cell. Similarly, the weighting scheme is employed to interpolate the potential gradients calculated on the mesh nodes to the particles. This scheme is as follows:

$$(\nabla \phi)_p = (\nabla \phi)_p + (\nabla \phi)_n \left(1 - \frac{|(z_n - z_p)\pi(r_n^2 - r_p^2)(\theta_n - \theta_p)|}{V_{cell}} \right) \quad (15)$$

By utilizing the weighting scheme, the total electric field on a macro particle is calculated with the contribution coming from the 8 nodes that constitute the cell that the particle is located.

The electric potential equation (11) is discretized according to the second order finite differencing scheme and the resulting coefficient matrix is solved using the ILU-preconditioned GMRES algorithm.

After the electric potential and the electric field are evaluated, the ions move according to the force applied on them. The particle motion is performed with the commonly used Leapfrog algorithm.¹⁸ According to this method, for each macro particle the following equations are valid:

$$\mathbf{r}_i = \mathbf{r}_{i-1} + \mathbf{v}_{i-\frac{1}{2}} \Delta t \quad (16)$$

$$\mathbf{v}_{i+\frac{1}{2}} = \mathbf{v}_{i-\frac{1}{2}} + \mathbf{a}_i \Delta t \quad (17)$$

$$\mathbf{v}_{\frac{1}{2}} = \mathbf{v}_0 + \mathbf{a}_0 \frac{\Delta t}{2} \quad (18)$$

Initial position of the particle is determined using a random number generator. The initial particle velocity is equal to the Bohm velocity in the axial direction. First iteration for the velocity is performed as presented in (18). During the particle movement only the acceleration is changed at each time step.

The acceleration is directly evaluated from the force applied by the electric field on the macro particles:

$$\mathbf{F} = q(\mathbf{v} \times \mathbf{B} + \mathbf{E}) = m\mathbf{a} \quad (19)$$

where the force due to the magnetic field is considered to be negligible in the vicinity of the grid. Especially in our case, RF ion thrusters, where the maximum induced magnetic field is on the order or 10 G, it is safe to leave out these terms.

With this simplification, a macro particle's acceleration is calculated as:

$$\mathbf{a} = \frac{q}{m} \mathbf{E} \quad (20)$$

As stated above, this acceleration value is found for each particle. But the electric field is evaluated on the nodes of the cell, not on the individual particles. Therefore, a reverse weighting scheme is necessary to

evaluate the electric field on each particle. For the initial acceleration, the Laplace equation is solved and the force is applied on the charged macro particles.

In order to obtain a correct simulation and to prevent divergence of numerical iterations, energy conservation for macro particles is applied explicitly. The particles are assumed to conserve their energy throughout the simulation domain:

$$E_{total} = \frac{1}{2}m|\mathbf{v}|^2 + q\phi \quad (21)$$

At the end of each time step, the energy of the macro particle is forced to remain constant by modifying the magnitude of the velocity vector:

$$v_{conserved} = \sqrt{\frac{2}{m}(E - q\phi)} \quad (22)$$

$$\alpha = \frac{v_{conserved}}{v} \quad (23)$$

$$v_{conserved} = \sqrt{(\alpha v_x)^2 + (\alpha v_y)^2 + (\alpha v_z)^2} \quad (24)$$

In the absence of charged particles in the field, the solution for the potential field is obtained as presented in Fig. 7. The electric field is calculated as the gradient of the potential:

$$\mathbf{E} = -\nabla\phi = -\left(\frac{\partial\phi}{\partial r}\hat{\mathbf{r}} + \frac{1}{r}\frac{\partial\phi}{\partial\theta}\hat{\boldsymbol{\theta}} + \frac{\partial\phi}{\partial z}\hat{\mathbf{z}}\right) \quad (25)$$

Collisions with the grid walls are handled so that particles colliding with the walls are reflected back into the system with the same momentum. The code implemented understands that a collision with grid walls occurred during the phase where the particles are relocated and reassigned to the cells they are located in. If a particle is found to be located in one of the grid cells, its location and velocity are changed accordingly.

Similarly, reflections from the radial and azimuthal boundaries are implemented so that the particles turn back into the system while retaining their momentum. This reflection scheme is performed as represented in Figure 4.

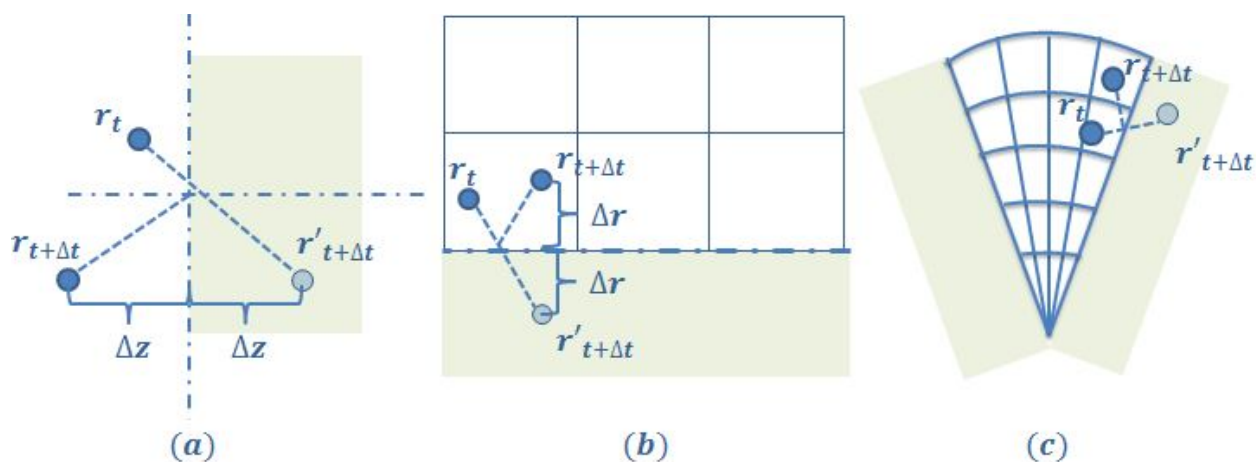


Figure 4. (a) Representation of the position change after axial reflection. (b) Representation of the position change after radial reflection from the center line. (c) Representation of the position change after azimuthal reflection from the center line

IV. Elastic DSMC Collisions

Collisions between particles are handled with the conventional DSMC approach, so that particles in a particular cell collide only with the ones in that cell. In our model there are ion and neutral particles. The collisions that can occur are as follows:

- Elastic collisions between neutrals

- Elastic collisions between ions and neutrals
- Charge-exchange (CEX) collisions between ions and neutrals

The probability of a collision to occur is calculated by using the collision cross-section and collided pair's relative speed. In collision mechanics, the collision frequency is proportional to three variables. These are the densities of the collision partners, the relative velocity of the colliding particles and the collision cross section. The collision frequency of a particle colliding with another one can be formulated as:

$$\nu = nc_r\sigma \quad (26)$$

where n denotes the effective number density, c_r is the relative speed, and σ is the collision cross section. The term σc_r has the units $[m^3/s]$ and denotes the volume swept out by the particle per second for the considered collision type. What this means is depicted in Fig. 5. In our model, the number density and the relative velocity with collision cross section are separated from each other during the handling of collisions. Particles colliding in our model belong to the same species, in this case Xenon, and they are represented by macro particles with a predetermined weight.

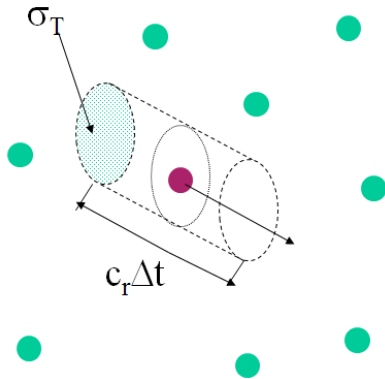


Figure 5. Representation of the effective volume swept by a moving particle

The probabilistic collision approach obtained in this model can be explained with an example. Suppose there are 40 ion and 60 neutral macro particles in a cell. The selection of the first particle is done among the neutrals since in all the collisions considered in this model at least one neutral must participate. First, a random fraction, R_1 is generated. Assume that this fraction, R_1 , is 0.32. Since $60 \times 0.32 = 19.2$, the first collision partner is the neutral with the index 19. To select the second partner, a second random fraction, R_2 is generated.

After the second particle is selected, there is a last step to determine whether the selected collision will occur with the selected particles. For this step, the collision frequency is evaluated and its ratio with the maximum collision frequency is calculated. If this ratio is larger than a random fraction, R_3 , then the collision occurs. This can be shown as:

$$r = \frac{\sigma c_r}{(\sigma c_r)_{max}} \quad (27)$$

where if $r > R_3$, the collision occurs, else the process is repeated. Depending on the type of the collision, this maximum value has a global constant that is valid for all cells.

Cross-sections for collisions can be specified as follows:

For Xe neutral and Xe ion elastic collisions:¹⁹

$$\sigma = (175.26 - 27.2 \log_{10}(c_r)) 10^{-20} \quad (28)$$

For Xe neutral and Xe ion charge exchange collisions, the collision cross-section is assumed to be equal to the neutral-ion collision cross-sections.²⁰

For Xe neutral and Xe neutral elastic collisions:

$$\sigma = 2.117 \times 10^{-18} \times c_r^{-0.24} \quad (29)$$

To determine how many collision attempts will be performed in a cell, the following formula is used:

$$N_{coll, Xe} = \frac{N_n(N_n - 1)}{2} W_n W_n \frac{(\sigma c_r)_{max, Xe}}{\Delta V_{cell}} \Delta t \quad (30)$$

$$N_{coll, Xe+} = N_n N_i W_n W_i \frac{(\sigma c_r)_{max, Xe+}}{\Delta V_{cell}} \Delta t \quad (31)$$

$$N_{coll, CEX} = N_n N_i W_n W_i \frac{(\sigma c_r)_{max, CEX}}{\Delta V_{cell}} \Delta t \quad (32)$$

where $N_{coll,Xe}$ is neutral-neutral elastic collision count, $N_{coll,Xe+}$ is the neutral-ion elastic collision count, and $N_{coll,CEX}$ is the charge-exchange collision count. N_n and N_i are the number of neutral and ion macro particle counts in the considered cell. W_i is the ion macro particle weight, and W_n is the neutral particle weight. ΔV is the volume of the considered cell, $(\sigma c_r)_{max,x,e}$, $(\sigma c_r)_{max,x,e+}$, and $(\sigma c_r)_{max,CEX}$ are the effective collision volume per second for values for neutral-neutral, neutral-ion, and CEX collisions, respectively.

The collision model described above can be verified by the analytical evaluation of the collision count that takes place inside a predetermined volume in a specified time step. The number of collisions between species p and q is calculated as:

$$n_p n_q \langle \sigma_{pq} c_r \rangle V \Delta t \quad (33)$$

where n_p and n_q represent the number density of both particle species in $[m^{-3}]$, V is the volume of the considered domain, Δt is the time interval in our consideration. σ_{pq} is the collision cross-section of the investigated collision type between species p and q .

The aim of the verification procedure is to compare the analytically evaluated collision count inside a confined region to the numerically evaluated collision count as performed previously in literature.²¹ The term in angled brackets, $\langle \sigma_{pq} c_r \rangle$, denotes the Maxwellian average of the collision cross-section multiplied by the relative velocity. This term is evaluated by taking the integral:

$$\langle \sigma c_r \rangle = \int \int F(\mathbf{v}_1) F(\mathbf{v}_2) \sigma c_r d\mathbf{v}_1 d\mathbf{v}_2 \quad (34)$$

For a container that has the same volume of the solution domain in our configuration and for the ion and neutral gas densities $n_i = n_n = 1.0e + 17 m^{-3}$, 26.13 Xe-Xe elastic collisions and 55.51 CEX and Xe-Xe⁺ elastic collisions should occur according to the formulation presented above at each time step, which is specified as 2.0e-09 seconds for convenience. The numerical implementation employed in this study yields 35.40 Xe-Xe elastic collisions and 46.40 CEX and Xe-Xe⁺ elastic collisions.

Collisions are handled using the Cartesian coordinate system, therefore the velocity components are converted first from cylindrical into Cartesian coordinate system, thus from (v_r, v_θ, v_z) to (v_x, v_y, v_z) . This conversion for both particles are performed according to the following formula:

$$v_x = v_r \sin(\theta) - r v_\theta \cos(\theta) \quad (35)$$

$$v_y = r v_\theta \sin(\theta) + v_r \cos(\theta) \quad (36)$$

$$v_z = v_z \quad (37)$$

For two particles with masses m_1 and m_2 , and with velocities \mathbf{c}_1 and \mathbf{c}_2 , the center of mass velocity is given by:

$$\mathbf{c}_m = \frac{m_1 \mathbf{c}_1 + m_2 \mathbf{c}_2}{m_1 + m_2} \quad (38)$$

The particles have the same mass and assumed to have the same macro particle factor. The center of mass velocity, c_m , of these particles are calculated as:

$$c_{m_x} = (v_{x_1} + v_{x_2})/2 \quad (39)$$

$$c_{m_y} = (v_{y_1} + v_{y_2})/2 \quad (40)$$

$$c_{m_z} = (v_{z_1} + v_{z_2})/2 \quad (41)$$

Also the relative velocity, c_r , and speed of the colliding particles are calculated:

$$c_{r_x} = (v_{x_1} - v_{x_2}) \quad (42)$$

$$c_{r_y} = (v_{y_1} - v_{y_2}) \quad (43)$$

$$c_{r_z} = (v_{z_1} - v_{z_2}) \quad (44)$$

$$|c_r| = \sqrt{c_{r_x}^2 + c_{r_y}^2 + c_{r_z}^2} \quad (45)$$

After calculating the center of mass velocity, relative velocity and speed, the impact factor and scattering angle for the collision are calculated using two random numbers:

$$\epsilon = 2\pi R_1 \quad (46)$$

$$\chi = \cos^{-1}(2R_2 - 1) \quad (47)$$

where R_1 and R_2 are the random numbers, ϵ denotes the impact angle and χ is the scattering angle in radians. Post-collision velocity components for each particle are calculated first by evaluating the post-collision relative velocity. Post-collision relative velocity is:

$$c'_{r_x} = c_{r_x} \cos(\chi) + \sqrt{c_{r_y}^2 + c_{r_z}^2} \sin(\chi) \sin(\epsilon) \quad (48)$$

$$c'_{r_y} = c_{r_y} \cos(\chi) + \sin(\chi) \left(\frac{|c_r| c_{r_z} \cos(\epsilon) - c_{r_x} c_{r_y} \sin(\epsilon)}{\sqrt{c_{r_y}^2 + c_{r_z}^2}} \right) \quad (49)$$

$$c'_{r_z} = c_{r_z} \cos(\chi) - \sin(\chi) \left(\frac{|c_r| c_{r_y} \cos(\epsilon) + c_{r_x} c_{r_z} \sin(\epsilon)}{\sqrt{c_{r_y}^2 + c_{r_z}^2}} \right) \quad (50)$$

The post-collision velocities are calculated using the post-collision relative velocity calculated as above. The formula for post-collision velocities are:

$$\mathbf{c}_1' = \mathbf{c}_m + \frac{m_2}{m_1 + m_2} \mathbf{c}_r' \quad \mathbf{c}_2' = \mathbf{c}_m - \frac{m_1}{m_1 + m_2} \mathbf{c}_r' \quad (51)$$

These formulations and their implementation vary slightly when the macro particles have different weighting factors. If β is the ratio of the macro particle factors:

$$\beta \leq W_I/W_N \quad (52)$$

where W_I and W_N are the macro particle factors for ions and neutrals, and β is a random number between 0 and 1. To take the difference between macro particle factors of neutrals and ions into account, after assigning post-collision velocities to the lower weight particles, the velocities are assigned also to higher-weight particles if the randomly generated number, β , is lower than the ratio of macro particle factors. Otherwise, another two collision pairs are selected and this procedure is repeated during the simulation for each time step and each collision pair.

V. Solution Domain and Computational Settings

The domain that is investigated within the scope of this work is depicted in Figure 6. The domain is 5 mm long in the axial direction, assuming that it starts from the downstream plasma discharge and extends until the upstream plume region. The purpose of the current study is to evaluate a relationship between the discharge plasma density and the beam current for a specific grid geometry. The geometric configuration depicted in Figure 6 is held to be same at all simulation runs for this study, and an optimization scheme to find the best geometric configuration for the desired beam current is left for future work.

The solution domain is divided into 62 x 62 x 10 nodes, which are in axial, radial and azimuthal directions, respectively. The only partial differential equation solved in the main algorithm is the Gauss' Law to evaluate the electric potential equation. This equation is discretized using the conventional second order finite differencing in cylindrical coordinates for three dimensions. The evaluated potential field is used to calculate the electric field on the computational cell nodes and these values are then interpolated to be acted upon each particle as the Lorentz force.

The solution domain considered for the initial runs is obtained from literature.⁶ The physical length of the domain in axial directions is 5 mm, and the radial length is 2 mm. The screen grid is set to 2241 V, the accelerator grid is set to -400 V, and the plume potential is set to 0 V. The upstream discharge plasma is assumed to be 2266 V, which corresponds to a 25 V potential difference between the grid wall and the discharge plasma. The radial and azimuthal boundaries have symmetry boundary conditions.

Each macro particle is marched in time and a loop over particles locates the cells where each particle is located in. Each cell object contains a neutral and an ion particle list. Cell objects also contain flags to indicate whether they correspond to screen or accelerator grids, or they are boundary cells at the edges of the computational domain in three directions. If a particle gets into these cells, it is reflected while retaining its momentum as depicted in Figure 4.

As stated previously, there are two macro particle types in the simulation: Ions and neutrals. Particles enter the system from the left boundary with Maxwellian averaged velocities. Even though in an ion thruster

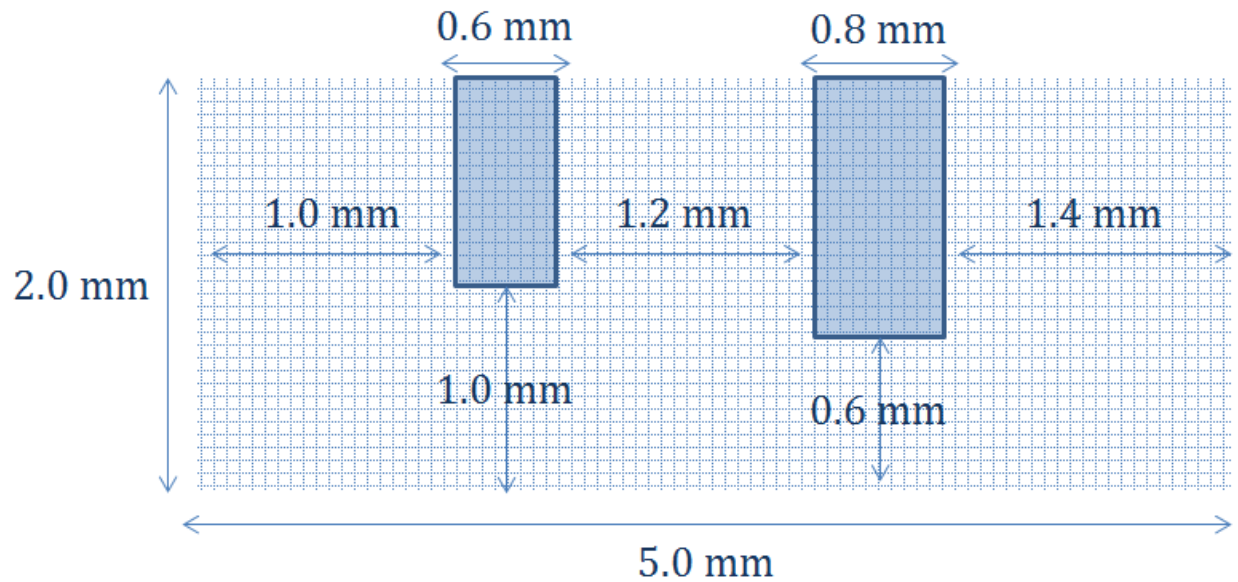


Figure 6. Dimensions of the solution domain for simulations

it is possible to make the cold gas assumption,²² which means that the heavy species of the same gas have the same temperature and therefore have the same thermal velocity, the acceleration due to the electric field requires to consider different time scales for ions and neutrals. A simple routine is developed to calculate the time step for a neutral-only simulation, which is performed to evaluate the steady-state neutral distribution for a particular geometry. The time step is arranged so that a particle can not march in time and cover a distance larger than Δz , which is the computational cell length in the axial direction. After the steady state for neutrals is reached, ions start to be fed into the system. When the ions enter the system, the time step is reduced to the amount that is required to track ions.

An object-oriented implementation is preferred using the C++ programming language. Particles and cells are initialized as *class* objects and *vector* type of containers is used to store and process them. The vector object's inherit functions, such as *push_back* and *erase*, are extensively utilized to initialize and delete particles. The code is compiled using Microsoft Visual C++, and multi-core parallelization is utilized where it is possible to speed-up the simulation.

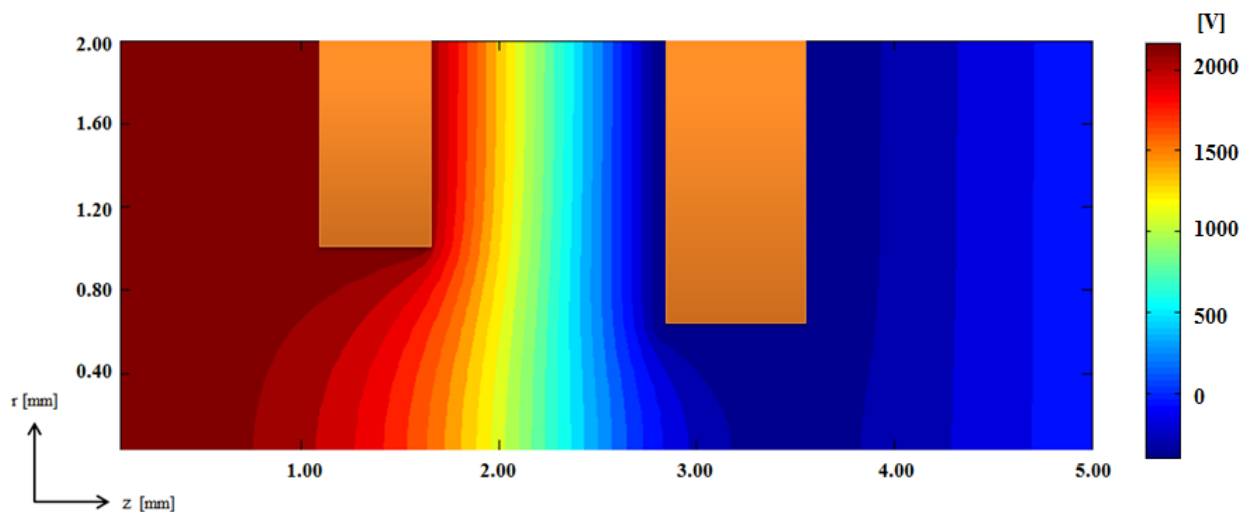


Figure 7. Electric potential fields in the solution domain at $t=0$ sec.

VI. Results

A series of simulations are performed to investigate the effects of the discharge plasma properties on the extracted beam current, and perveance for a particular grid geometry. The varied parameters between cases are the ion number density and the electron temperature. The incoming macro particle count, N , at each time step is calculated with the following formula:

$$N = \frac{nv_{inlet}A_s\Delta t}{W} \quad (53)$$

where A_s is the inlet surface boundary area, and v_{inlet} is the inlet velocity. For ions v_{inlet} is calculated with the drifted Maxwellian distribution, where the drift velocity is equal to the Bohm velocity. The positive charge density, which constitutes the RHS of the Gauss' Law, is directly proportional to the total amount of ions, which can be expressed as $\rho_i = N_iW_i/\Delta V$. Increasing the incoming ion density has therefore a direct effect on the evaluated electric potential.

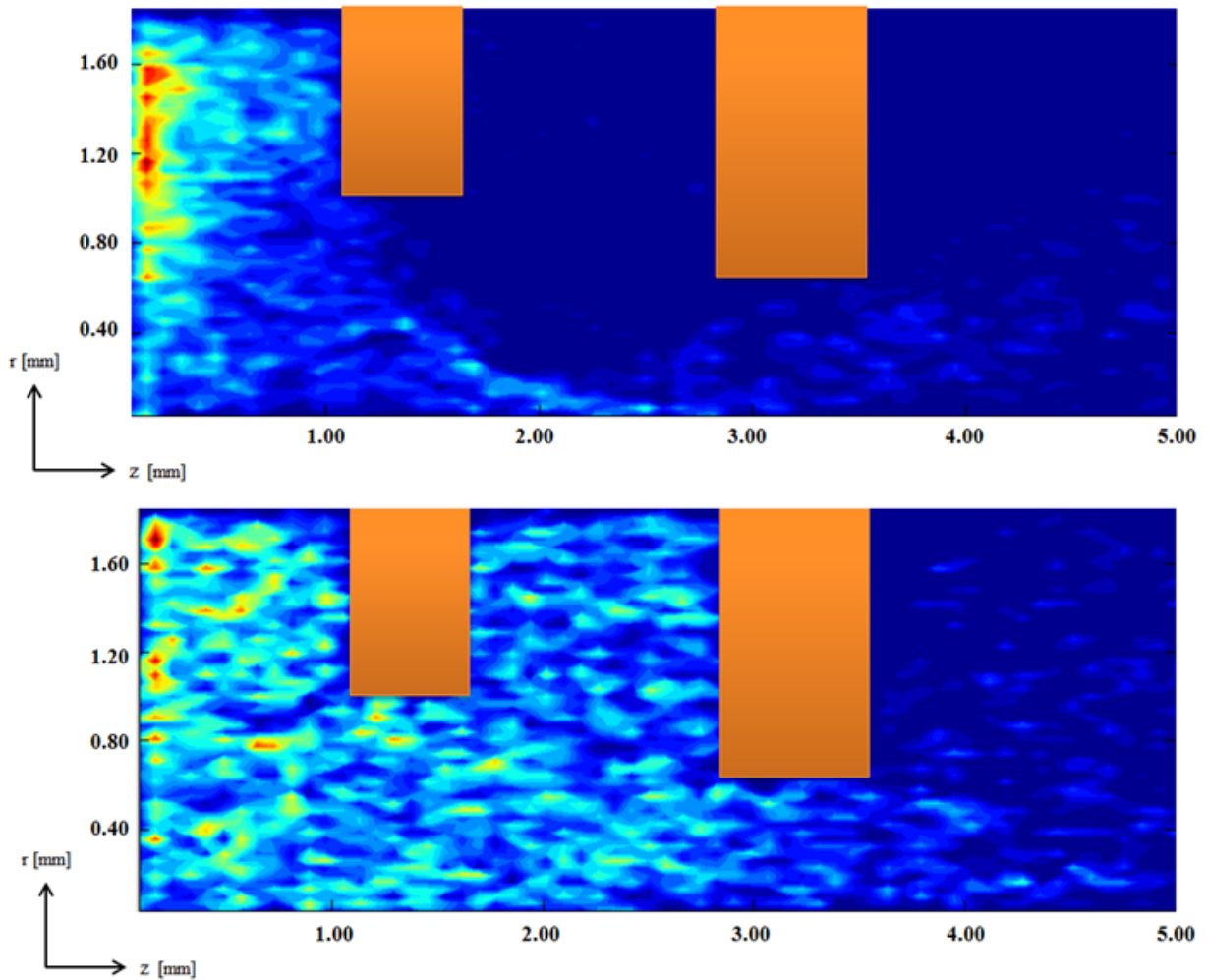


Figure 8. Steady state ion (top) and neutral (bottom) particle density distributions

Initially, while no ions are present in the system, the Gauss' Law reduces to the form of the Laplace's equation, where the RHS of Equation 11 goes to zero. For this problem ILU-GMRES linear solver converges in 0.795 seconds on a dual processor 3.30 GHz Intel Xeon workstation. ILU-GMRES is proven to be the most efficient solver among Jacobi, Gauss-Seidel and not preconditioned GMRES solvers. The resulting electric potential field is depicted in Figure 7. This solution indicates the existence of an almost uniform axial electric field between the screen and accelerator grids. It is observed that the axial component of the

electric potential gradient is much larger compared to the radial component of the electric potential gradient as expected.

The electric potential distribution shows a 25 V potential difference between the inlet and the front of the screen grid. Ions that enter the system fall from this 25 V potential difference approximately for the 1.0 mm after the upstream boundary. Then, they fall from a 2666 V potential difference along 2.00 mm up to the end of the acceleration grid. After that there is a 400 V *potential uphill* up to the end of the accelerator grid and the plume region.

According to the electric potential distribution depicted in Figure 7, if all the potential energy can be converted into the kinetic energy, the maximum ion velocity can be calculated as:

$$\frac{1}{2}m_i v_{Bohm}^2 + qV = \frac{1}{2}m_i v_{max}^2 \quad (54)$$

$$v_{max} = \sqrt{\frac{2}{m_i} \left(\frac{1}{2}m_i v_{Bohm}^2 + qV \right)} \quad (55)$$

where V is the maximum potential difference that an ion can undergo, and q is the charge of the single ion particle. For the example configuration presented in the literature,⁶ taking the upstream temperature as 1.5 eV, and the maximum potential difference as 2666 V, the calculated velocities are:

$$v_{Bohm} = 1051 \text{ m/s} \quad v_{max} = 62676 \text{ m/s} \quad (56)$$

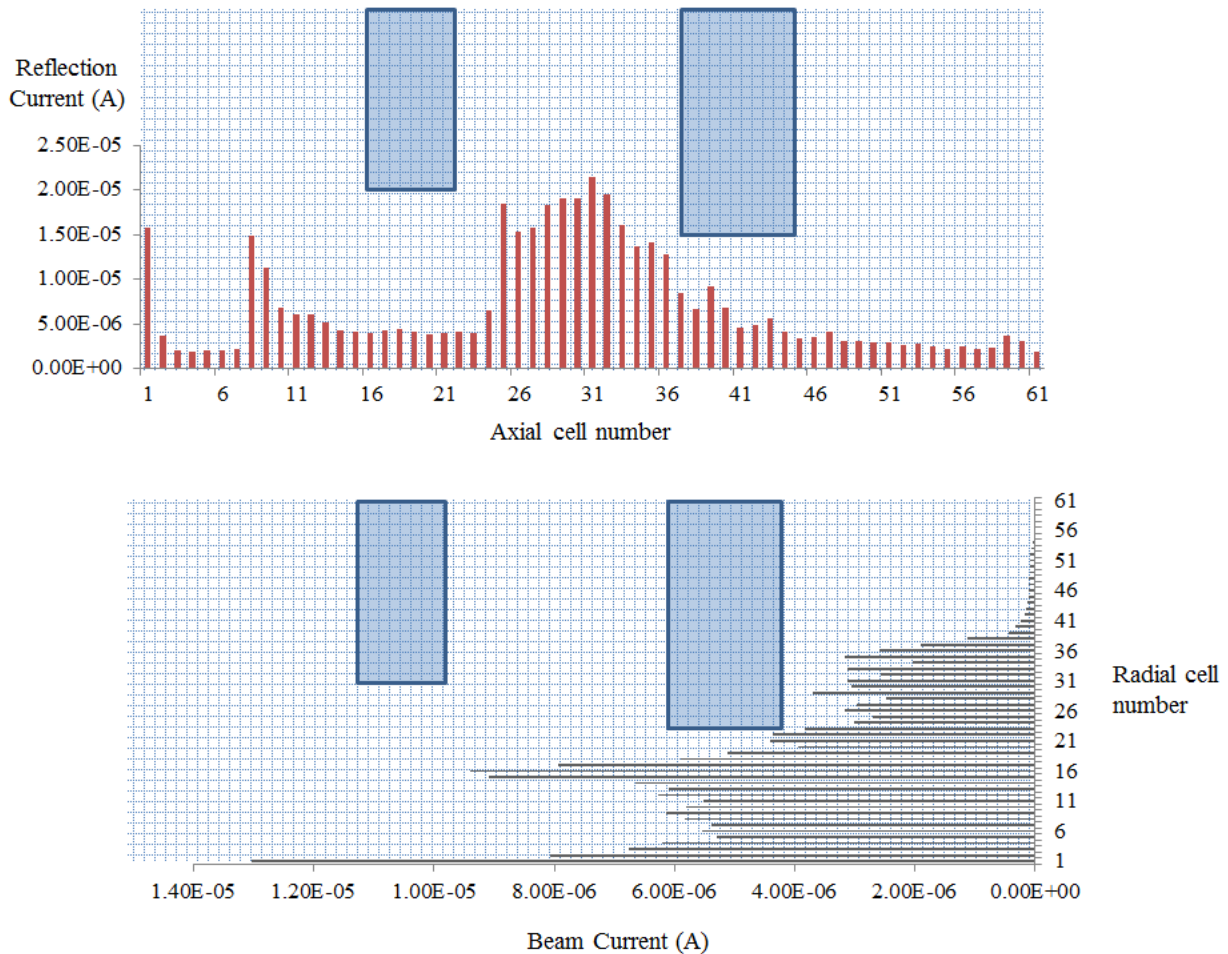


Figure 9. Distributions of the reflection current from the center line (top) and the exit plane beam current (bottom) for the discharge plasma ion number density: $n_i = 1.0e + 16$

When an ion particle enters the system, its potential energy is so high that the inlet velocity does not play an important role in determining the outlet velocity of the particle. Therefore, the first impression tells us that the discharge plasma temperature does not play an important role at determining the ion current obtained from the thruster. But as the simulation marches in time, it is observed that the incoming ions start to behave as electrostatic barriers by contributing to the electric potential and changing the direction of the electric field at the upstream of the domain. When the electric field direction is reversed, only the particles that enter the system with sufficient kinetic energy can overcome this potential barrier.

Another factor that may depend on the discharge plasma properties is the perveance of the system. Perveance denotes the *flatness* of the beamlet coming out of the grid hole, such that the particles should be kept from crossing center line or hitting the grid walls as much as possible. The steady-state ion and neutral distributions are plotted in Figure 8. For this case the upstream plasma temperature is 1.5 eV, incoming ion density is $1.0e+16 \text{ m}^{-3}$ and incoming neutral density is $1.0e+17 \text{ m}^{-3}$. Incoming neutral density is kept constant throughout this study. From the ion number density distribution depicted in that figure, it can be observed that the ions are reflected from the center line around $z = 2.20 \text{ mm}$. The neutral number density, on the other hand, shows an almost linear variation in axial direction. It is observed to be maximum at the upstream region and it decreases towards downstream. This trend of neutral density agrees with those presented in literature.⁶

The perveance can be investigated by evaluating the reflected current from the center line numerically. Same logic can be applied also to calculate the beam current extracted from the grid hole. The current passing through any boundary can be expressed as:

$$I_{cell} = \frac{eN_iW_i}{\Delta t} \quad (57)$$

where the evaluated current I_{cell} gives the current through a computational cell. In this formula N_i is the number of ion macro particles that pass through a certain boundary. By keeping track of the center line and the axial domain edge, the reflection and beam current values are evaluated. The current values passing through each computational cell for radial center line reflection and for beam current are presented in Figure 9 for the bulk plasma density $n_i = 1.0e + 16 \text{ m}^{-3}$. In the top figure, the radial center line reflection current is depicted. It is observed that the reflection current is maximum around the middle of the center line. It is also seen that the first cell has an abnormally high reflection, this reflection is due to the fact that the particles may be reflected right after they enter the domain if their radial velocity is in negative direction.

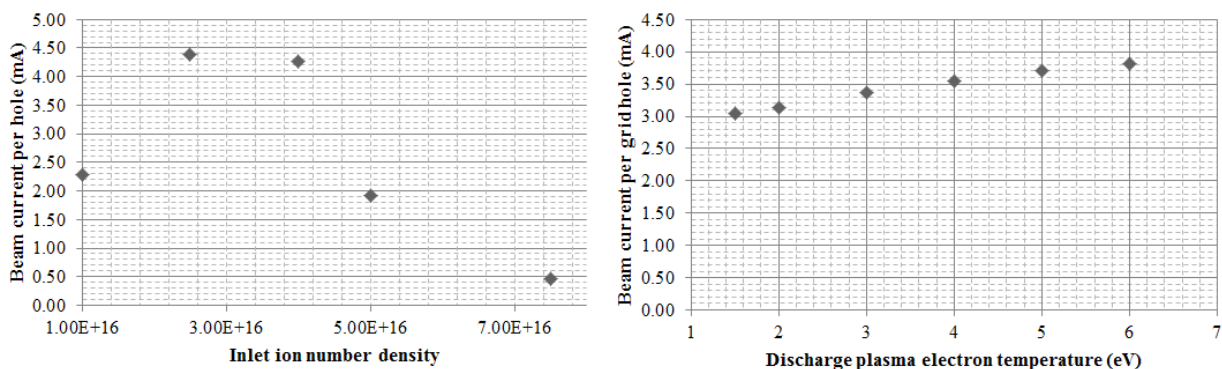


Figure 10. Change in the beam current per hole with changing inlet ion number density and discharge plasma electron temperature

The bottom plot in Figure 9 shows the distribution of the beam current among computational cells. The optimum profile for minimum beam divergence would have a linearly decreasing trend from the center line towards the upper radial boundary. In the current case, the cell adjacent to the center line has the highest amount of ions passing through it. It is also seen that there is almost no current leaving from the upper portions of the exit plane.

For the investigated $n_i = 1.0e + 16 \text{ m}^{-3}$ case, the beam current per grid hole is calculated as 2.28 mA. The change of the beam current per hole is investigated with different inlet ion number density and discharge plasma electron temperature values while keeping all other parameters constant at each case. The results are

depicted in Figure 10. The plot on the left, which shows the results while keeping the electron temperature constant at $T_e = 1.5$ eV, indicates that the beam current does not vary linearly with increasing inlet ion number density as would be expected if the space charge effect was negligible. Even though the beam current increases at the initial runs with lower inlet ion number densities, an electrostatic wall effect is observed as the inlet number density is increased. For the excessive inlet ion number density conditions, it is observed that the ions that enter the domain are reflected back because of the reverse electric field acting on them.

The plot on the right in Figure 10 shows the results of simulations where the electron temperature is changed from 1.5 eV to 6.0 eV while holding the inlet ion number density constant at $n_i = 1.5e + 16$ m⁻³. It is observed from this set of results that even if the discharge plasma temperature is changed drastically, the beam current does not show significant variation without modifying the plasma number density.

VII. Conclusion

A simulation platform to be used in the design ion thruster accelerator grids for the studies in BUST-Lab is developed. The motion of macro particles is handled using the cylindrical coordinates in three-dimensions. DSMC collisions are implemented with elastic collision cross sections obtained from literature. Three types of heavy species collisions, Xe-Xe elastic, Xe-Xe⁺ elastic, and CEX collisions, are implemented. The solution domain is chosen so that it represents the smallest symmetric section of a two-grid system that is manufactured in a hexagonal pattern with circular concentric grid holes.

It is evaluated that the space charge effects are crucially important at designing an ion thruster accelerator grid system. For a particular design it is possible that beam current falls drastically, because the excess of ions disturbs the electric potential field and creates an electrostatic wall in front of the ions.

The effect of the plasma electron temperature is demonstrated to be very limited compared to the effect of the plasma number density. A drastic temperature increase from 1.5 eV to 6.0 eV causes only an increase on the order of 30%. Therefore it can be said that to increase the beam current, the efforts can be directed to increasing the beam number density rather than increasing the electron temperature, while considering the space charge effects and the resulting electrostatic wall for ions.

The model will need more capabilities to simulate ion optics physics more accurately. Currently double-ions are neglected, but they should be included into the system for the configurations where double-ions constitute a considerable ratio among the charged species. The code also currently does not track electrons. Future work should include the handling of the electrons and a Full-PIC simulation of ion optics grids. Besides the code currently does not model sputtering, which is a key factor in thruster lifetime.

The code is implemented using the C++ programming language and uses the object oriented programming extensively. The future work should include the parallelization of the solution of the Poisson's equation through domain decomposition for faster simulations in three dimensions.

Acknowledgment

This work was supported in part by The Scientific and Technological Research Council of Turkey under Projects TUBITAK-112M862 and TUBITAK-113M244 and in part by Bogazici University Scientific Research Projects Support Fund under Project BAP-6184 and BAP-8960.

References

- ¹Goebel, D. M. and Katz, I., *Fundamentals of Electric Propulsion - Ion and Hall Thrusters*, JPL Space Science and Technology Series, 2008.
- ²Yavuz, B., Turkoz, E., and Celik, M., "Prototype design and manufacturing method of an 8 cm diameter RF ion thruster," *6th International Conference on Recent Advances in Space Technologies (RAST)*, IEEE, 2013, pp. 619–624.
- ³Turkoz, E. and Celik, M., "2D Fluid Model for Axisymmetric RF Ion Thruster Cylindrical Discharge Chamber," *49th Joint Propulsion Conference*, San Jose, CA, July 2013, also AIAA-2013-4110.
- ⁴Wilbur, P. J., Beattie, J. R., and Hyman, J., "Approach to the parametric design of ion thrusters," *Journal of Propulsion and Power*, Vol. 6, No. 5, 1990, pp. 575–583.
- ⁵Beattie, J., "A Model for Predicting the Wearout Lifetime of the LeRC/Hughes 30 cm Mercury Ion Thruster," *14th International Electric Propulsion Conference*, Princeton, NJ, October 1979.
- ⁶Farnell, C., "Performance and Lifetime Simulation of Ion Thruster Optics," Ph.D. Dissertation, Colorado State University, Fort Collins, CO, USA, 2007.

⁷Anderson, J. R., Katz, I., and Goebel, D., *Numerical simulation of two-grid ion optics using a 3D code*, Pasadena, CA: Jet Propulsion Laboratory, National Aeronautics and Space Administration, 2004.

⁸Brophy, J. R., Katz, I., Polk, J. E., and Anderson, J. R., "Numerical simulations of ion thruster accelerator grid erosion," *AIAA Paper*, Vol. 4261, 2002, pp. 2002.

⁹Nakayama, Y. and Wilbur, P. J., "Numerical Simulation of High Specific Impulse Ion Thruster Optics," *27th International Electric Propulsion Conference*, Pasadena, CA, 2001, also IEPC-01-099.

¹⁰Wirz, R. E., Anderson, J. R., and Katz, I., "Time-Dependent Erosion of Ion Optics," *Journal of Propulsion and Power*, Vol. 27, No. 1, 2011, pp. 211–217.

¹¹Kuninaka, H., "Research and development of JIEDI (JAXA ion engine development initiatives) tool for numerical evaluation of ion engine grid lifetime," *JAXA special publication*, 2007, pp. 5–9.

¹²Nakano, M., "Doubly charged ion effect on life prediction accuracy of ion acceleration grid system," *Vacuum*, Vol. 88, 2013, pp. 70–74.

¹³Oh, D. Y., "Computational Modeling of Expanding Plasma Plumes in Space Using a PIC-DSMC Algorithm," Ph.D. Thesis, Massachusetts Institute of Technology, Cambridge, MA, USA, 1996.

¹⁴Fife, J. M., "Hybrid-PIC Modeling and Electrostatic Probe Survey of Hall Thrusters," Ph.D. Thesis, Massachusetts Institute of Technology, Cambridge, MA, USA, 1999.

¹⁵Szabo, J. J., "Fully Kinetic Numerical Modeling of a Plasma Thruster," Ph.D. Thesis, Massachusetts Institute of Technology, Cambridge, USA, 2001.

¹⁶Celik, M., Santi, M. M., Cheng, S. Y., Martinez-Sanchez, M., and Peraire, J., "Hybrid-PIC Simulation of a Hall Thruster Plume on an Unstructured Grid with DSMC Collisions," *28th International Electric Propulsion Conference*, Toulouse, France, March 2003, also IEPC-03-134.

¹⁷Rovang, D. C. and Wilbur, P., "Ion Extraction Capabilities of Two-Grid Accelerator Systems," *Journal of Propulsion and Power*, Vol. 1, No. 3, 1985, pp. 172–179.

¹⁸Fox, J. M., "Advances in Fully-Kinetic PIC Simulations of a Near Vacuum Hall Thruster and Other Plasma Systems," Ph.D. Thesis, Massachusetts Institute of Technology, Cambridge, USA, 2007.

¹⁹Miller, J. S., Pullins, S. H., Levandier, D. J., Chiu, Y.-h., and Dressler, R. A., "Xenon charge exchange cross sections for electrostatic thruster models," *Journal of Applied Physics*, Vol. 91, No. 3, 2002, pp. 984–991.

²⁰Huismann, T. and Boyd, I., "Advanced Hybrid Modeling of Hall Thruster Plumes," *46th Joint Propulsion Conference and Exhibit*, 2010.

²¹Cheng, S., Santi, M., Celik, M., Martinez-Sanchez, M., and Peraire, J., "Hybrid PIC-DSMC simulation of a Hall thruster plume on unstructured grids," *Computer Physics Communications*, Vol. 164, No. 1, 2004, pp. 73–79.

²²Tsay, M., "Two-Dimensional Numerical Modeling of Radio-Frequency Ion Engine Discharge," Ph.D. Thesis, Massachusetts Institute of Technology, Cambridge, MA, USA, 2011.